Dielectric study of the interplay between charge carriers and electron energy losses in reduced titanium dioxide

Rémi Lazzari,* Jingfeng Li, and Jacques Jupille
CNRS, Sorbonne Université, Institut des NanoSciences de Paris, UMR 7588, 4 Place Jussieu, F-75005 Paris, France

(Received 14 April 2018; revised manuscript received 4 June 2018; published 27 August 2018)

The transport mechanism in titanium dioxide through polarons is an open issue. High-resolution electron energy-loss spectroscopy (HREELS) is in principle of great relevance in such context, provided the fingerprints on the loss spectrum of the charge carriers involved in the material are disclosed. This paper aims at evidencing those fingerprints. Through a suitable parametrization of the dielectric function, a theoretical analysis of EELS excitations in defective TiO_2 rutile is developed in the framework of the semiclassical dielectric theory. The focus is put on the interplay between phonons, interband transitions, and defect-related excitations, namely, plasmon and band-gap states. Transport properties are demonstrated to be more efficiently grasped through the screening they induce on phonons than through the existence of a defined surface plasmon peak. While the corresponding imaginary part of the dielectric function only yields a slight broadening and temperature dependence of the quasielastic peak due to the large static dielectric function and electron effective mass, a sizable upward shift in energy and a decrease in intensity of phonons due to the real part are predicted. Band-gap states also screen phonons but with downward shift in energy loss. Due to its large oscillator strength, the high-energy-lying surface phonon at 95 meV is a very sensitive reporter of the combined effects of transport behavior and band-gap states. Finally, it is highlighted that extracting quantitative information out of EELS experiments requires an accurate modeling of the depth profile.

DOI: 10.1103/PhysRevB.98.075432

I. INTRODUCTION

The behavior of the excess electrons present in titania and their link with the (photo)catalytic properties of the oxide have triggered a substantial amount of fundamental studies [1–9], in particular at the prototypical (110) surface of rutile. Created by photon adsorption, doping or through intrinsic stoichiometric defects such as oxygen vacancies or titanium interstitials, they formally correspond to a change of oxidation state from Ti^{4+} to Ti^{3+} by populating states derived from the conduction band. Due to the large static dielectric function of TiO_2 rutile [10], they are accompanied by a strong lattice polaronic distortion that screens them giving rise to specific fingerprints depending on the way they are excited [11–13]. On the one hand, excess electrons appear as band-gap states (BGS) if the lifetime of the excitation is shorter than the phononic relaxation. In reduced TiO_2, BGS related to defects [1–8] are evidenced by (i) a photoemission line at 0.8–1 eV below the Fermi level E_F [14–17] that reverberates in Auger transitions involving the valence band [18], (ii) an electron energy loss of $\sim$1 eV [19–22], (iii) features in scanning tunneling spectroscopy [23,24], or (iv) near-infrared absorption [25,26] and electron spin-resonance band [27]. On the other hand, transport measurements [28–31] favor a conduction mechanism through polarons, the radius of which remains an open issue [32]. According to simulations, large polaron or freelike carriers in the conduction band seem to compete with more localized polaronic configurations in TiO_2 rutile [24,33,34]. Up to now, the dual character of excess electrons has never been evidenced within the same experiment, not to speak about the possible coexistence of trapped and free states that would account for transport and spectroscopic measurements.

High-resolution electron energy-loss (HREELS) [35,36] deserves attention in such context. Aside from vibrational analysis of adsorbates, HREELS has proved its capabilities to probe solid-state excitations in the surface region of materials since the birth of the technique [37]. Loss fingerprints of phonons, plasmons, band-to-band transitions, and gap states have been described in the dipolar scattering regime [35,38]. Numerous studies have already shown the sensitivity (i) to surface plasmon, in particular in space-charge layers at the surface of semiconductors, and (ii) to the coupling of those excitations to phonons as in ZnO(0001) [39–42], Si(111) [43–45], InSb(110) [46,47], InAs(110) [48], and GaAs(100) [49–51]. In most cases, physical parameters related to the profile of carrier concentration were derived by applying the dielectric theory [35,52–58]. Although blurred by multiple excitations and by a complex in-depth sensitivity, HREELS intrinsically probes dielectric properties in a way similar to optics with the advantage of covering a wide range of energy at once. The earlier HREELS experiments that were performed in the 1980's on rutile [19,20,59] and anatase [60] addressed the question of phonon spectra and pinpointed the existence of a defect-related band-gap feature. Since then, several groups have explored the defect reactivity with probe molecules (H_2O [61], O_2 [62–64], CO [65], HCOOH [42], etc. …) by looking at (i) either the evolution of the corresponding stretching frequencies (ii) or the variation of the BGS intensity. In line with the infrared study of Baumard and Gervais [66,67], the first HREELS

*Corresponding author: remi.lazzari@insp.jussieu.fr

experiments on TiO_2 [19,20,59] have stressed the existence of a relationship between the defect-related BGS and the conductivity although they pointed to intrinsic limitations of the HREELS technique that prevented in-depth exploration. Rocker *et al.* [19] suspected that "the modification in intensity and frequency of Fuchs-Kliewer phonons may be correlated with concentration of free electrons near the surface"; but they "could not resolve plasmon excitations at low energies due to the linewidth of the instrument and the background of phonons near the elastic peak." Later on, Eriksen and Edgell [20,59] focused only on the "downward shift and attenuation of the highest-energy phonon loss that was attributed to modification of the effective background dielectric constant by defect excitations (BGS)." In association with Cox and Flavell [59], the previous authors even tried to simulate the phonon spectra within the dielectric theory; but they were "unable to reproduce the observed changes of intensity without introducing an unduly large downward shift in phonon energy." The lack of a solution to overcome these limitations likely explains that since that time and despite the burst of interest in charge localization in TiO_2 (see reviews [2–9]), the correlation between the defect-related BGS and the conductivity has no longer been addressed by the HREELS technique. While the n-type conductivity of reduced TiO_{2-x} is used to perform measurements, the existence of collective excitations due to carriers in EELS has never been disclosed although the sizable carrier concentration obtained by reduction [31] should lead to an EELS signature as in the case of more conventional semiconductors [35].

To relaunch the debate, this work aims at analyzing theoretically the capability of HREELS in correlating transport and BGS. This paper is built as follows. After a reminder of the used dielectric theory of EELS (Sec. II), a suitable dielectric function including all the solid-state excitations in reduced TiO_2 from infrared to ultraviolet is proposed (Sec. III). Then, the impact of carrier absorptions and band-gap states on the quasielastic peak (Sec. IV A) and the phonon excitation (Secs. IV B and IV C) is analyzed theoretically by stressing on the effect of screening. Beyond the exploration of specific fingerprints for the various excitations that exist in the surface region of the oxide, new prospects are opened on interplays between those excitations. The role of the relative probing depth as a function of energy loss is also developed (Sec. V).

II. REMINDER ON DIELECTRIC THEORY OF EELS AND METHODS

All simulations have been performed within the semiclassical dielectric theory [35,52–58], the relevance of which in the modeling of EELS spectra has been proven since the early beginning of the technique [37] and in depth over the years [38,68].

In an EELS experiment, an electron of charge $-e$, mass m_e, wave vector $\mathbf{k}_I$, incident energy $E_I = \hbar^2 k_I^2/2m_e$, and velocity $\mathbf{v}_I = \hbar\mathbf{k}_I/m_e$ impinges on the sample surface at an angle Θ_I before being scattered along the direction given by wave vector $\mathbf{k}_S$. In the following, the subscripts $\parallel$ and $\perp$ stand for components parallel and perpendicular to the surface, respectively. In the standard dipole scattering theory, the electron is assumed to be a classical particle that follows a nearly unperturbed specular trajectory, i.e., $k_\parallel = |\mathbf{k}_{\parallel,I} - \mathbf{k}_{\parallel,S}| \ll k_I$, and bounces off the surface giving rise to a transient electrostatic field that produces excitations in the substrate. The single-loss probability for an electron inelastically scattered in an energy window $\hbar d\omega$ around $\hbar\omega \ll E_I$ and close to the specular direction reads as [35,52–58]

$$P_{cl}(\mathbf{k}_I,\omega) = \frac{4e^2}{\hbar v_\perp}\int_D \frac{(k_\parallel v_\perp)^3}{[(\omega-\mathbf{k}_\parallel.\mathbf{v}_\parallel)^2+(k_\parallel v_\perp)^2]^2} \times \mathrm{Im}\left[-\frac{1}{1+\xi(\mathbf{k}_\parallel,\omega)}\right]\frac{d^2\mathbf{k}_\parallel}{k_\parallel^2} = \int_D F(\mathbf{k}_I,\omega)G(k_\parallel,\omega)d^2\mathbf{k}_\parallel, \quad (1)$$

where $\hbar$ is the Planck constant divided by 2π and $v_\parallel = v_I \sin\Theta_I$, $v_\perp = v_I\cos\Theta_I$. The $\mathbf{k}_\parallel$ integration domain D in Eq. (1) is defined by the incident beam divergence and detector angular acceptance, the so-called slit integration [35]. To avoid the cumbersome [69] underlying fourth integral over incoming/scattering angles for convergent/divergent beams, the present analyses have been performed with an equivalent circular detector acceptance θ_c and a parallel incident beam. In that case, $\mathbf{k}_\parallel$ depends on θ_S ($0 < \theta_S < \theta_c$), the small angle from the specular direction and on ϕ_S, the azimuth angle looking downwards the origin [22,35],

$$\mathbf{k}_\parallel = k_I \begin{cases} -\theta_S\cos\phi_S\cos\Theta_I + \theta_E\sin\Theta_I, \\ -\theta_S\sin\phi_S \end{cases} \quad (2)$$

with $\theta_E = \hbar\omega/2E_I$. If the integrand in Eq. (1) depends only on the modulus of $k_\parallel$, the sum over (θ_S,ϕ_S) in Eq. (1) can be transformed into a one-dimensional radial integral in the $\mathbf{k}_\parallel$ plane (see Appendix of Ref. [58] for details), a process that speeds up calculations. $P_{cl}(\mathbf{k}_I,\omega)$ involves two terms. On the one hand, the kinematical prefactor or sensitivity function $F(\mathbf{k}_I,\omega)$ gives rise to the angular behavior of the EELS cross section with an intense lobe of aperture θ_E close to the specular direction [35] and a fast decay with $\hbar\omega$. On the other hand, the loss function $G(k_\parallel,\omega)$ depends on the effective dielectric function $\xi(\mathbf{k}_\parallel,\omega)$ of the probed interface which, for a homogeneous isotropic nondispersive semi-infinite substrate is nothing else than the dielectric function of the medium $\epsilon(\omega)$. Indeed, since the present analyses have been mainly performed in the specular direction, no intrinsic $\mathbf{k}_\parallel$ dependence (i.e., dispersive behavior of the dielectric function [70]) has been accounted for. For a uniaxial material like TiO_2, $\xi(\mathbf{k}_\parallel,\omega)$ depends in a complex way on the relative orientation of the crystallographic axis and of the scattering plane [57] (see Sec. S1 in Supplemental Material [71]). Hopefully, when the c axis (or [001]) of the quadratic structure is perpendicular (respectively, parallel) to the scattering plane, $\xi(\mathbf{k}_\parallel,\omega) \simeq \epsilon_\perp^a(\omega)$ [respectively, $\xi(\mathbf{k}_\parallel,\omega) \simeq \sqrt{\epsilon_\perp^a(\omega)\epsilon_\parallel^c(\omega)}$] becomes $\mathbf{k}_\parallel$ independent. It is given by the two components of the dielectric tensor $\epsilon_\parallel^c(\omega)$ and $\epsilon_\perp^a(\omega)$ along directions parallel and perpendicular to the c axis.[1] As detailed in Sec. S1 of Supplemental Material [71], Eq. (1) can be generalized to account recursively

[1]The notations $\parallel$, $\perp$ of the components of the dielectric tensor and of the scattering geometry have different meanings.

for any profile of dielectric function along the normal to the surface [58].

When the coupling between the incident electron and the medium is relatively strong or when the energy loss is of the same order of magnitude as kT as in the case of surface plasmons, the single scattering probability Eq. (1) breaks down. The spectrum involves a complex combination of intense multiple energy losses and gains due to the creation and annihilation of quanta of excitations [37]. The problem at hand can be treated completely (i) on quantum-mechanical point of view either in the first Born approximation or in a more complex way including multiple scattering [54,55] or (ii) through a semiclassical method by considering the electron as a classical source of perturbation for the quantized boson field of surface excitations [35,52,70]. Within this more tractable approach, the HREELS spectrum $P(\omega)$ at finite temperature T including multiple excitations is generated through

$$P(\omega) = \frac{1}{2\pi}\int e^{-i\omega t}\mathcal{R}(t)e^{[\mathcal{P}(t)-\mathcal{P}(0)]} \tag{3}$$

$$= e^{-\mathcal{P}(0)}R(\omega)\otimes\left\{\delta(\omega)+\sum_{n=1}^{\infty}\frac{1}{n!}[\mathcal{P}(\omega)]^{n\otimes}\right\}, \tag{4}$$

$$\mathcal{P}(t) = \int_0^{+\infty} d\omega' P_{cl}(\omega') \tag{5}$$

$$\times[(n_{\omega'}+1)(e^{i\omega' t}+1)+n_{\omega'}(e^{-i\omega' t}-1)], \tag{6}$$

where $n_\omega = [e^{\hbar\omega/k_B T}-1]^{-1}$ is the Bose-Einstein distribution, k_B the Boltzmann constant, $\otimes$ the convolution product. $\mathcal{P}(t)$ and $P(\omega)$ are related by Fourier transform. In order to simulate a finite resolution of the spectrometer by a convolution, an instrumental transfer function $\mathcal{R}(t) = \int e^{-i\omega t}\mathcal{R}(\omega)d\omega$ can be easily introduced before the back Fourier transform in Eq. (3). The EELS spectrum $P(\omega)$ appears as the multiple convolution [Eq. (4)] of the single gain-loss function $\mathcal{P}(\omega)$ which generates not only multiple losses from a given transition, but also combination features between different transitions and also gain peaks at finite temperature. The series of multiple losses follows a Poisson statistics [Eq. (4)] [37,72]. Finally, the $\mathbf{k}_\parallel$ integration over domain D has been restricted herein to one-quantum loss processes, i.e., performed on $P_{cl}(\mathbf{k}_I,\omega)$ [Eq. (1)] and not on the multiple excitation cross section $P(\omega)$ [Eq. (3)] as it should be [70]. But, the underlying approximation is usually hidden in the experimental uncertainties [70].

On a practical point of view, once the function $\xi(\mathbf{k}_\parallel,\omega)$ is defined from the profile of the dielectric function (see Sec. S1 in Supplemental Material [71]), $P_{cl}(\Theta_I, E_I, \omega)$ [Eq. (1)] is obtained by one-dimensional (1D) autoadaptative numerical integration [73] under the symplifying assumption of a circular detection slit [58]. It is then Fourier transformed after multiplication by the required Bose-Einstein statistics [Eq. (6)] for the selected temperature T to obtain $\mathcal{P}(t)$ [Eq. (5)]. The exponential of this latter is then multiplied by the Fourier transform of the apparatus point spread function $\mathcal{R}(t)$ before being back Fourier transformed to obtain the final simulated HREELS spectrum $P(\omega)$. In passing, a great care has been taken in the sampling in the integrals in Eqs. (1), (5), and (6) which may be biased by numerical issues at low plasmon energies or dampings. Fast Fourier transform was used with an energy step down to $\Delta\hbar\omega = 10^{-4}$ meV. If not stated afterward, the following simulation parameters corresponding to experiments [22,69] have been used throughout this theoretical study: beam energy $E_I = 8$ eV or $E_I = 38$ eV; incident angle $\Theta_I = 60°$; circular aperture in detection $\theta_c = 1°$; Gaussian shape for the apparatus resolution function [74] $\mathcal{R}(\omega) = \frac{1}{\sigma_a\sqrt{2\pi}}\exp[-\frac{\hbar^2\omega^2}{2\sigma_a^2}]$ with a full-width at half-maximum (FWHM) of $\Delta_a = 2\sqrt{2\ln(2)}\sigma_a = 8$ meV for HREELS at $E_I = 8$ eV or $\Delta_a = 50$ meV for EELS at $E_I = 38$ eV; temperature $T = 300$ K. Simulations have been performed with a beam perpendicular to the c axis, i.e., with a dominant contribution from $\epsilon_\perp^a(\omega)$. If not specified, simulations involve hereafter only a semi-infinite substrate; profiles of dielectric function treated in Sec. V have been sliced in a staircase way to compute recursively $\xi(\mathbf{k}_\parallel,\omega)$ until reaching convergence of the simulated spectrum.

III. DIELECTRIC FUNCTION OF TiO_2 FROM INFRARED TO ULTRAVIOLET

An accurate expression of the two components $\epsilon_\parallel^c(\omega)$ and $\epsilon_\perp^a(\omega)$ of the dielectric tensor of TiO_2 is required to model the energy-loss spectrum of TiO_2 over a large spectral range (up to 6 eV). To obtain a tractable analytic expression of the dielectric function, $\epsilon_\parallel^c(\omega)$ and $\epsilon_\perp^a(\omega)$ have been decomposed into contributions due to phonon $\epsilon_{Ph}(\omega)$, band-to-band transitions $\epsilon_{Ib}(\omega)$, band-gap states $\epsilon_{gs}(\omega)$, and Drude or plasmonlike excitations $\epsilon_{Pl}(\omega)$ (Fig. 1):

$$\epsilon_{TiO_2}(\omega) = \epsilon_{Ph}(\omega)+\epsilon_{Ib}(\omega)+\epsilon_{gs}(\omega)+\epsilon_{Pl}(\omega). \tag{7}$$

As seen in what follows, the two former components of the equation can be extracted from tabulated data. However, new approaches are required to determine the contribution $\epsilon_{gs}(\omega)+\epsilon_{Pl}(\omega)$. If not stated specifically, the labels $\parallel, \perp$ for the dielectric function are assumed to be implicit hereafter. Each term of Eq. (7) will be detailed one after the other. Since only dipolar EELS simulations will be carried out ($k_\parallel \simeq 0$), any dependence on wave-vector transfer parallel to the surface $k_\parallel$, i.e., nonlocal effects, can be safely discarded.

A. Phonons

As suggested in the infrared reflectivity analysis of Gervais and Piriou [67,76,77] and in the accurate mid-infrared and far-infrared ellipsometric measurements of Schöche *et al.* [10], the contribution of infrared-active optical phonons is described through a factorized model:

$$\epsilon_{Ph}(\omega) = \epsilon_{Ph,\infty}\prod_n \frac{\omega_{\mathrm{LO},n}^2-\omega^2-i\Gamma_{\mathrm{LO},n}\omega}{\omega_{\mathrm{TO},n}^2-\omega^2-i\Gamma_{\mathrm{TO},n}\omega}. \tag{8}$$

ω_{LO}, ω_{TO} and Γ_{LO}, Γ_{TO} stand for the frequencies and dampings of the longitudinal and transverse phonon modes at the center of the Brillouin zone. $\epsilon_{Ph,\infty}$ is the optical dielectric function, i.e., at frequencies much higher than phonons. The used parameters from Ref. [10] given in Table S1 of Supplemental Material [71] match perfectly with all previous determinations of phonon modes in rutile via infrared probe [76,78], neutron scattering [79], and *ab initio* modeling [80–82]. This infrared ellipsometry analysis [10] was performed on stoichiometric TiO_2

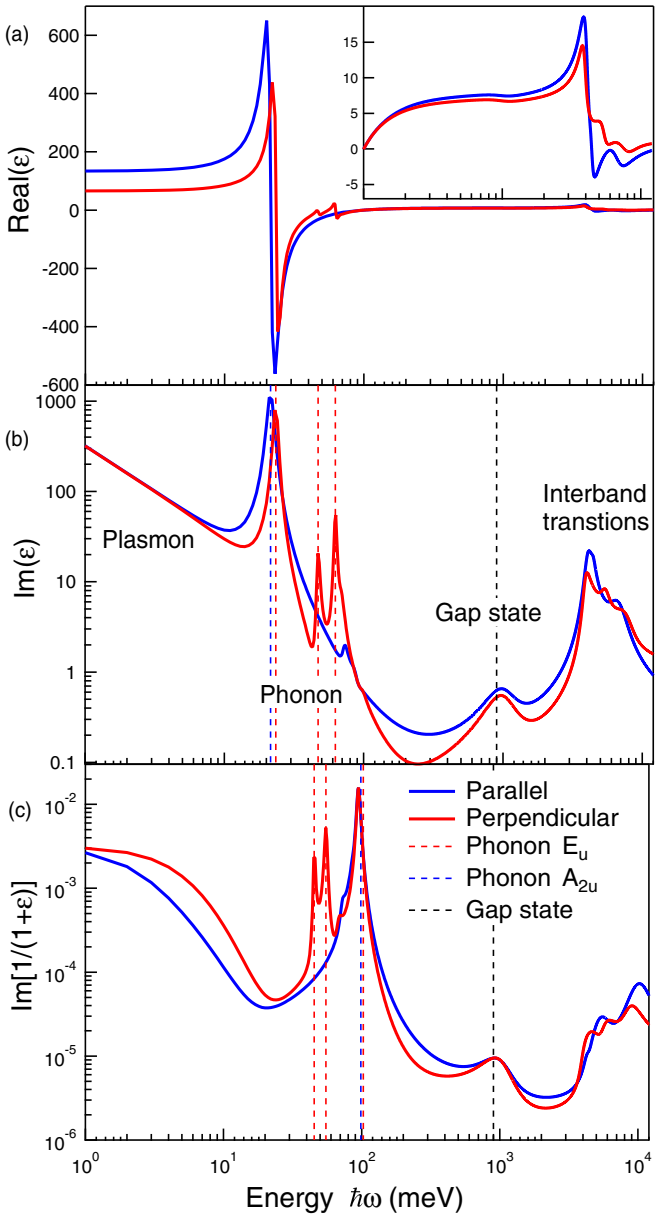

FIG. 1. (a) Real and (b) imaginary parts of the TiO_2 dielectric functions $\epsilon^c_{\parallel}(\omega)$ (blue line), $\epsilon^a_{\perp}(\omega)$ (red line) [Eq. (7)]. (c) Corresponding loss function $\mathrm{Im}[1/1+\epsilon(\omega)]$. The inset shows a zoom of $\mathrm{Re}[\epsilon(\omega)]$ over the 0.1–12 eV range. Vertical dotted blue and red lines pinpoint the frequencies of transverse ω_{TO} [Fig. 1(b)] and longitudinal ω_{LO} [Fig. 1(c)] phonons frequencies of bulk TiO_2 used in $\epsilon_{Ph}(\omega)$ [Eq. (8)]. $\hbar\omega_p = 80$ meV, $\hbar\Gamma_P = 20$ meV, $\hbar\omega_{gs} = 1000$ meV, $\hbar\Gamma_{gs} = 600$ meV, $\hbar\Omega_{gs} = 500$ meV have been used to describe the Drude [Eq. (12)] and band-gap states [Eq. (11)] contributions; the phonon and interband transition counterparts are extracted from Refs. [10] and [75], respectively. The black dotted line points at the position of BGS.

samples [83] of various orientations (001), (110), and (111). The group theory decomposition in irreducible representation of TiO_2 rutile phonons [20,79,80,84] (point group D^1_{4h} or $P4/mmm$): $\Gamma = A_{1g} + A_{2g} + A_{2u} + B_{1g} + B_{2g} + 2B_{1u} + E_g + 3E_u$ shows that only four modes $(A_{2u} + 3E_u)$ have infrared (EELS) dipole activity with longitudinal/transverse splitting. E_u modes are doubly degenerated. Therefore, the summation in Eq. (8) extends over $n_{\perp} = 3\,E_u$ and $n_{\parallel} = 1\,A_{2u}$ modes. The factorized form of $\epsilon(\omega)$ was preferred over the classical summation of damped oscillators [20,78] to allow independent broadenings of transverse and longitudinal phonons and asymmetric shapes as observed in ionic crystal with several modes having large TO-LO splitting [10,76,77]. Furthermore, it explicitly expresses the longitudinal phonon frequencies probed in transmission EELS as the poles of $1/\epsilon_{Ph}(\omega)$. In reflection EELS, Fuchs-Kliewer modes [35,37] appear as the maxima of (i) $\mathrm{Im}[1/(1+\epsilon_{\perp,Ph}(\omega)]$ at $\hbar\omega_{\mathrm{sph},1} = 45.3$ meV, $\hbar\omega_{\mathrm{sph},2} = 54.6$ meV, $\hbar\omega_{\mathrm{sph},3} = 95.4$ meV and (ii) of $\mathrm{Im}[1/(1+\sqrt{\epsilon_{\parallel,Ph}(\omega)\epsilon_{\perp,Ph}(\omega)}]$ at $\hbar\omega_{\mathrm{sph},1} = 45.6$ meV, $\hbar\omega_{\mathrm{sph},2} = 55.4$ meV, $\hbar\omega_{\mathrm{sph},3} = 93.8$ meV for incident planes perpendicular and parallel to the c axis, respectively (Fig. S1 in Supplemental Material [71]). The similarity of the two sets of frequencies stems from the accidental degeneracy of $A_{2u,\parallel}$ and $E_{u,\perp}$ [20,59]. Four symmetry forbidden additional phonons of much lower oscillator strengths, two along each direction, have also been reported [10,76] (Table S1 and Fig. S2 in Supplemental Material [71]). They correspond to maxima in the phonon density of states and are probably activated by bulk defects through folding of the Brillouin zone. For completeness, they were accounted for in this study.

The severe longitudinal/transverse splitting of phonon modes in rutile (Table S1 in Supplemental Material [71]) results in large values of static dielectric constants. The Lyddanne-Sachs-Teller relation [85]

$$\epsilon(0) = \epsilon_{Ph,\infty} \prod_n \frac{\omega^2_{\mathrm{LO},n}}{\omega^2_{\mathrm{TO},n}} \tag{9}$$

leads to $\epsilon^c_{\parallel}(0) = 153$ and $\epsilon^a_{\perp}(0) = 84.7$ [10,76] in agreement with capacitance measurements [86]. Those values demonstrate the importance of the electron-phonon coupling that is at the origin of polaronic behavior of excess electrons. As a matter of comparison, $\epsilon(0)$ of ZnO wurtzite and Si are one order of magnitude lower [$\epsilon_{\mathrm{ZnO}}(0) = 8.7$; $\epsilon_{\mathrm{Si}}(0) = 11.7$].

B. Interband transitions

The valence and conduction bands of TiO_2 rutile are dominated by O sp and strongly localized Ti $3d$ states, respectively, with a direct Γ-point band gap of 3.1–3.2 eV [82,87,88] and a complex role of crystal-field effect on anisotropy at large energies [89,90]. The UV-visible contribution $\epsilon_{Ib}(\omega)$, in particular the part related to interband transitions, was extracted from the compilation of Ref. [75]. For the sake of EELS simulation, it was parametrized and fitted using the critical point transition approach [91]:

$$\epsilon_{Ib}(\omega) = \epsilon_{Ib,\infty} + \sum_m \left\{ \frac{C_m e^{i\Phi_m}}{(\omega_m - \omega - i\Gamma_m)^{\mu_m}} + \frac{C_m e^{-i\Phi_m}}{(\omega_m + \omega + i\Gamma_m)^{\mu_m}} \right\}. \tag{10}$$

$\epsilon_{Ib,\infty}$, C_m, Φ_m, μ_m, ω_m, Γ_m, are the high-frequency dielectric function and the amplitude, the phase, the pole order, the frequency, the damping of the mth critical point, respectively. Compared to the standard oscillator [92], this

representation accounts for transitions between band pairs with a substantial integration over k space leading to an apparent broadening larger than intrinsic linewidth and to functional dependence other than simple poles. A satisfactory fit in the 0.6–12 eV range of data of Ref. [75] (Fig. S3 in Supplemental Material [71]) was achieved with only three transition points along the parallel and perpendicular directions and zero phases (Fig. 1). Data were carefully matched to the $\epsilon_{Ph}(\omega)$ value from Ref. [10].

C. Defect-induced band-gap states and optical absorption

The BGS correspond to the optical absorption by a polaronic trapping state due to defect-related excess electrons, a polaron being a quasiparticle made of an electron and the accompanying phonon cloud due to lattice distortions. The slow motion of the atoms allows to freeze the self-trapping potential well during photoemission [12], which explains why thermal activation energy [28–31] differs from optical transition energy for excess electrons. The line shape of absorption from polaronic states depends on the degree of electron-phonon coupling, on the temperature or even on the dimensionality of space [93,94]. Two extreme cases can be distinguished: large and small polarons [11]. The photoionization of the hydrogenoic ground state of the potential well of the large polaron excites electrons to a continuum of unbound states. The absorption coefficient $\alpha \sim (kR)^3/\omega[1+(kR)^2]^4$, where $\hbar k = \sqrt{2m(\hbar\omega - 3E_p)}$ is the free-carrier wave vector and R the radius of the polaron, leads to a peaked asymmetric function that starts above three times the polaron binding energy E_p. Conversely, the self-trapped carrier of the small polaron is excited from its localized state to an adjacent site. The absorption coefficient $\alpha \sim \exp[-(2E_b - \hbar\omega)^2/\Delta^2]/\omega$ depends on the polaron binding energy E_b and on the thermal broadening Δ of levels. It shows a Gaussian line shape with an asymmetry on the higher-energy side and a strong temperature dependence in contrast to the large polaron model.

Aside from the debate on the location of excess charges in the subsurface region of TiO_2 [17,95–98], little is known about their degree of localization [22,24,33,99], i.e., the polaron radius. The large polaron model is favored in anatase [24,100,101]. The polaron radius is not settled yet in rutile [24,34,67], although the small polaron model is currently favored in bulk [25,102] and at (110) surfaces [103]. The apparatus sensitivity function and the actual profile of excess electrons to which several types of defects contribute [22] makes difficult the determination of the polaron radius via the asymmetry of the BGS in EELS. Therefore, it has been chosen herein to represent BGS optical absorptions by a simple oscillator model:

$$\epsilon_{gs}(\omega) = \frac{\Omega_{gs}^2}{\omega_{gs}^2 - \omega^2 - i\Gamma_{gs}\omega}, \tag{11}$$

where $\omega_{gs}, \Gamma_{gs}, \Omega_{gs}$ are the frequency, damping, and strength of the oscillator, respectively. This form is supposed to grasp most of the physics of screening discussed hereafter.

D. Excitation due to itinerant motion of carriers: Drude model

Reduced rutile is indubitably an n-type semiconductor whose transport properties have been much studied [30,31,104]. But their nature is unclear. In particular, the puzzling question of the large mobility [24,34] at low temperature is not understood, not speaking about the role of defects [22] (oxygen vacancies and/or titanium interstitials). Is transport in titanium dioxide due to a dual behavior of excess electrons or to the coexistence of trapped and free states giving rise to BGS and conductivity [24,34]?

Because of the strong electron-phonon coupling, transport is often debated in terms of the impact of the above-described small and large polarons on conductivity [24,34,67]. The ability of a polaron to move coherently in an alternative field is always restricted as it is linked to the atomic motion. However, a polaron can have a Drude-type carrier absorption [11,93,94] at low frequency if it moves itinerantly with a mean-free path greater than the intersite separation. For a large polaron, the Drude-type behavior occurs only at frequencies below the characteristic phonon frequency involved in the trapping. For a small polaron, the condition is more stringent. The extremely narrow bands that characterize small polaronic carriers may preclude itinerant (coherent) small-polaron motion in all but the most idealized conditions [11].

To account for EELS findings [69], the carrier excitations and therefore the conductivity at low frequency are described in this work through a classical Drude formula

$$\epsilon_{Pl}(\omega) = -\frac{\omega_P^2}{\omega^2 + i\omega\Gamma_P} \quad \text{with} \quad \omega_P^2 = \frac{ne^2}{m_e m^* \epsilon_0}, \tag{12}$$

where the plasma frequency ω_P is given in terms of the carrier density n and their effective polaronic mass m^*, (e, m_e, ϵ_0) being, respectively, the elementary electric charge, the electron rest mass, and the vacuum permittivity. The damping Γ_P is related to the carrier mobility μ through $\Gamma_P = 2\pi e/(m_e m^* \mu)$. The Drude model is the ground level of description of the frequency-dependent (or optical) conductivity $\sigma(\omega)$ [$\epsilon(\omega) = \epsilon_0 + i\sigma(\omega)/\omega$] through a collision relaxation time [85]. Baumard and Gervais [66,67] demonstrated that this basic model correctly fits the infrared reflectivity behavior in heavily reduced samples TiO_{2-x} ($x \simeq 0.001$–0.05) over a large frequency range (25–375 meV) well above the transverse optical frequency of phonons. They found that plasmons couple to longitudinal phonon modes and that ω_P^2 depends linearly on reduction level x. Through temperature-dependent measurements, they concluded that the activation of carriers to the conduction band constitutes the essential feature of the electrical conductivity. Frequency-dependent conductivity below the terahertz (4 meV) were also successfully interpreted with the Drude approach for optically created carriers [32,105] as well as for hydrogen doping [106] at low temperature. By using the Drude model, Hendry *et al.* [32,105] concluded that transport occurs through a polaron in the intermediate regime of coupling, neither large nor small with a strong anisotropy of effective mass and electron mobility.

IV. INTERPLAY BETWEEN EXCITATIONS IN REDUCED TiO_2

The energy losses that stem from carrier-related collective excitations have never been disclosed, although a fingerprint of conductivity is to be expected. The case is now explored by simulating (HR)EELS spectra of TiO_2(110) at low and

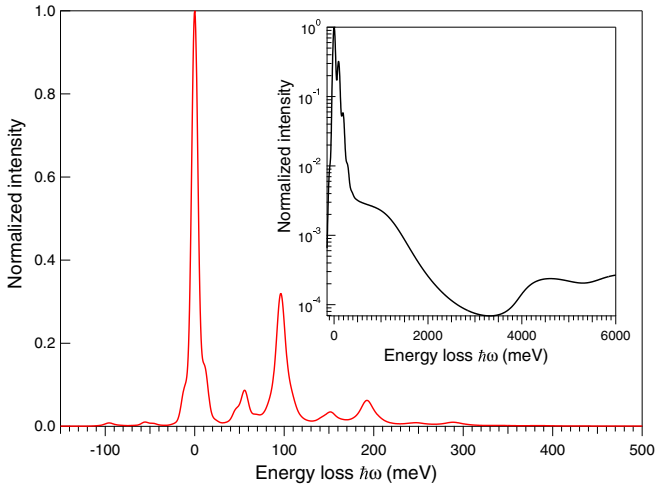

FIG. 2. An example of simulated HREELS spectrum in the region of phonons ($E_I = 8$ eV and $\Delta_a = 8$ meV) and of the interband transitions (inset: $E_I = 38$ eV and $\Delta_a = 50$ meV). The beam is perpendicular to the c axis for which the effective dielectric function amounts only to $\xi(\omega) = \epsilon^a_\perp(\omega)$ (Sec. II). Due to a fortuitous degeneracy of phonon modes [20,59], the crystal orientation at 90° leads to a similar spectrum (Sec. S2 in Supplemental Material [71]). Calculations include plasmon ($\hbar\omega_P = 120$ meV, $\hbar\Gamma_P = 2$ meV) and BGS ($\hbar\Omega_{gs} = 1000$ meV, $\hbar\omega_{gs} = 1000$ meV, $\hbar\Gamma_{gs} = 600$ meV) excitations.

large impact energies on the basis of the above-described dielectric function. The main features of such spectra are exemplified in Fig. 2. Aside from the single-phonon excitations $\omega_{\mathrm{sph},1}$, $\omega_{\mathrm{sph},2}$, $\omega_{\mathrm{sph},3}$ already present in the loss function [Fig. 1(c) and Fig. S2 in Supplemental Material [71]], multiple and combination excitations are accounted for as well as gain peaks on the negative energy-loss axis. Due to the sensitivity function $F(\mathbf{k}_I, \omega)$ (Sec. II), intensities of the elastic peak and phonon losses are several orders of magnitude higher than that of interband transitions located above 3.2 eV (inset of Fig. 2). Gap states appear clearly as an isolated broad feature in the EELS spectrum of reduced TiO_2 [20–22]. In the following, through dielectric simulations with typical experimental parameters, this section aims to identify the EELS signatures of the various excitations of excess electrons, including the interplay of the surface plasmons with the quasielastic peak and the screening of phonons by either carrier excitations or band-gap states.

A. Quasielastic peak broadening and surface plasmons

When low-frequency conductivity is described only through a Drude term $\epsilon(\omega) = \epsilon(0) - \omega_P^2/(\omega^2 + i\omega\Gamma_P)$, the classical loss function, which reads as

$$G(\omega) = \mathrm{Im}\left[-\frac{1}{1+\epsilon_{Pl}(\omega)}\right] = \frac{1}{1+\epsilon(0)}\frac{\Gamma_P\omega_{sp}^2\omega}{\left[\omega_{sp}^2-\omega^2\right]^2+\Gamma_P^2\omega^2}, \quad (13)$$

has a nearly Lorentzian shape that peaks at the so-called surface plasmon frequency $\omega_{sp} = \omega_P/\sqrt{1+\epsilon(0)}$. These excitations are coherent delocalized electron oscillations that exist at the interface between materials (vacuum/solid here). They are the electronic equivalent of surface phonons [35,107].

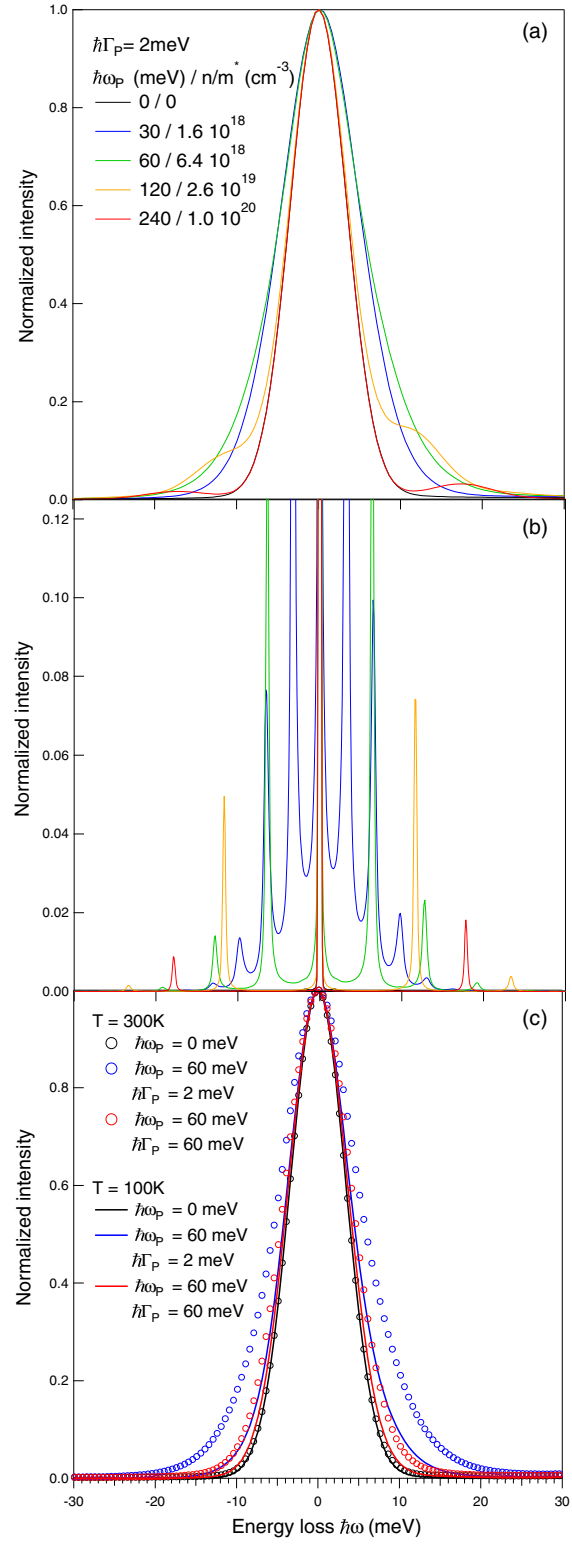

FIG. 3. Elastic peak shape (a) for selected plasmon frequencies ω_P (or carrier density n/m^*) at fixed damping $\hbar\Gamma_P = 2$ meV and room temperature, (b) at reduced damping $\hbar\Gamma_P = 0.25$ meV and increased apparatus resolution $\Delta_a = 0.25$ meV ($T = 300$ K), and (c) at two different temperatures $T = 100$ and 300 K for plasma frequencies ω_P, Γ_P given in figure.

For doped semiconductors, the conductivity manifests itself in EELS either as a isolated peak or as a broadening of the elastic peak due to multiple ω_{sp} excitations [35,43]. The coupling to the incident electrons may be so intense that the peak is better named "quasielastic" as nearly all reflected electrons suffer from energy loss. As an incipient ferroelectric compound, TiO_2 possesses a much higher static dielectric function $\epsilon(0)$ [$\epsilon_{\parallel}^{c}(0) = 153$, $\epsilon_{\perp}^{a}(0) = 84.7$, see Sec. III A] than ZnO and Si [$\epsilon_{\mathrm{ZnO}}(0) = 8.7$, $\epsilon_{\mathrm{Si}}(0) = 11.7$] of which surface plasmon excitation and accumulation/depletion layers have been studied by EELS [40–51]. In addition, the polaronic nature of the electronic transport leads to a much higher effective mass of $m^* = 8$–10 [31,32,67] than the estimate by *ab initio* band-structure calculations for a rigid lattice ($m_{\perp}^{a,*} = 1.1$, $m_{\parallel}^{c,*} = 0.57$ [82]). The combination of the two effects yields a $\omega_{sp} \sim 1/\sqrt{m^*}\sqrt{1+\epsilon(0)}$ value two orders of magnitude lower than for classical semiconductors at a given carrier concentration n (see top scales of Fig. 4). Consequently, the limited experimental resolution makes difficult the direct EELS detection of surface plasmon in TiO_2. Only a broadening of the quasielastic peak is expected.

Full numerical simulations of the elastic peak shape have therefore been carried out herein to identify both the effect of carrier concentration n/m^* and damping Γ_P on the FWHM of the quasielastic peak of rutile (Fig. 3). Aside from instrumental broadening Δ_a, the FWHM is driven by the superposition of multiple excitations of surface plasmons ω_{sp}, which are better visible when Γ_P and Δ_a values are artificially reduced [Fig. 3(b)]. Their intensities follow a Poisson distribution [Eqs. (3) and (4)] modulated by the Bose-Einstein statistics [Eq. (6)]. As predicted by the analytic formula of Ref. [43] (dotted line of Fig. 4, Sec. S3 in Supplemental Material [71]), increasing the carrier concentration results in a broadening of the quasielastic peak up to a turnover point at which a high enough surface plasmon frequency ω_{sp} [Fig. 4(a)] forms an isolated single excitation [Figs. 3(a) and 3(b)] that appears as a side shoulder of the elastic peak. In parallel, the quasielastic maximum follows the reverse trend. It decreases before the turnover point and then increases up to a value higher than that of a carrier-free substrate [Fig. 4(b)] which translates the increase of the elastic contribution to the quasielastic peak. Indeed, the progressive metallization of the substrate increases the fraction of elastically scattered electrons (inset of Fig. 4) given theoretically [35] by $e^{\mathcal{P}(t=0)}$ [Eq. (3)].

As shown in Fig. 4 when using a typical experimental resolution of $\Delta_a = 8$ meV, increasing Γ_P at fixed carrier density n/m^* surprisingly sharpens the quasielastic peak down to the resolution function. Notably, the discrepancies between the present simulations and the analytic formula of the broadening of quasielastic peak of Ref. [43] [Sec. S2 in Supplemental Material [71] and dotted black lines in Figs. 4(a) and 5] demonstrate its inadequacy in the present case due to the failure of infinitesimal Γ_P and ω_{sp}.

Finally, a temperature dependence of the elastic peak is found, in line with experimental findings [69], which results from a complex interplay between damping an carrier density (Fig. 5). Indeed, despite the existence of a possible combination of phonon modes at $\hbar\omega_{\mathrm{sph},2} - \hbar\omega_{\mathrm{sph},1} = 9.2$ meV, the elastic peak without carrier contribution ($\omega_P = 0$) should be insensitive to temperature (Fig. 3, black curve and circles).

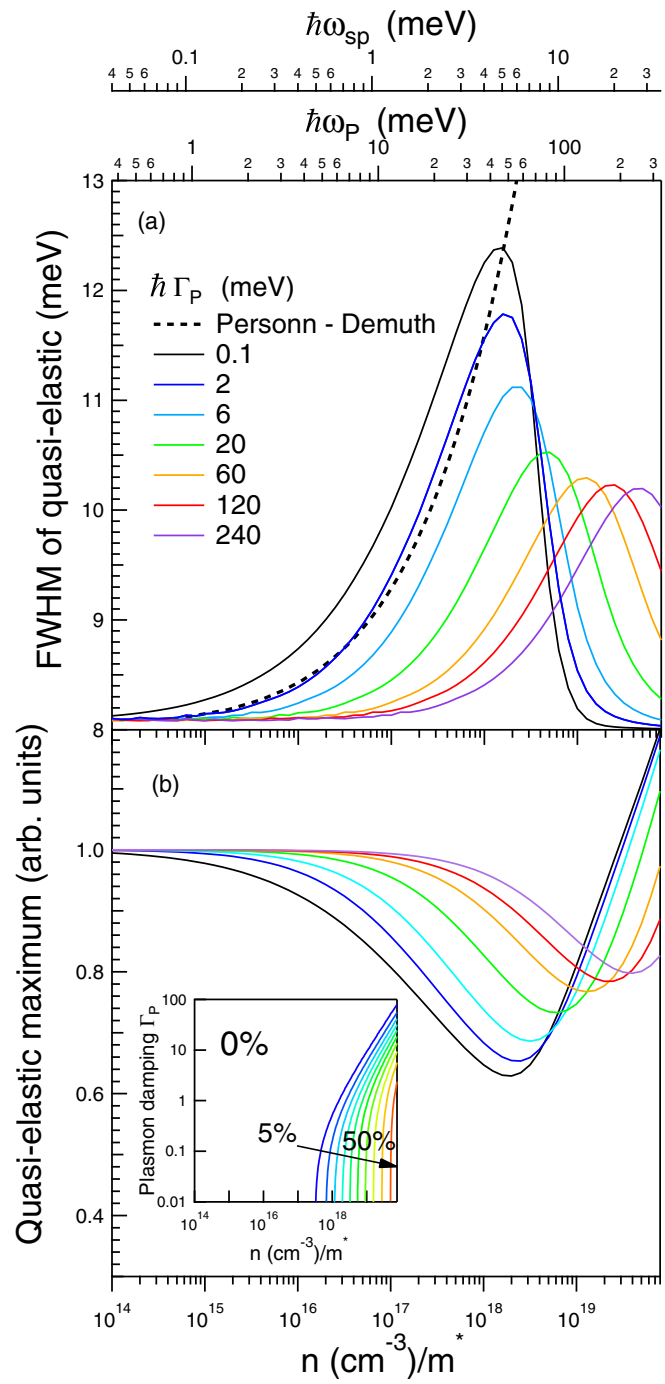

FIG. 4. (a) FWHM and (b) maximum of the quasielastic peak at $T = 300$ K as obtained from a simulated spectrum including multiple excitations [Eqs. (1)–(6)]. Quantities are plotted as a function of (i) carrier density n normalized by the effective mass m^* (bottom scale) or (ii) the bulk plasmon ω_P or surface plasmon ω_{sp} frequency (top scales) for various carrier plasmon dampings Γ_P. The comparison with the analytic formula Eq. (S3) in Supplemental Material [71] (dotted black line) is added for completeness in (a). The inset of (b) shows the fraction of elastically scattered electrons versus carrier density and damping.

B. Screening of phonons by carrier excitations

The plasmon-phonon coupling was addressed by Baumard and Gervais [66,67] in their infrared study of samples with

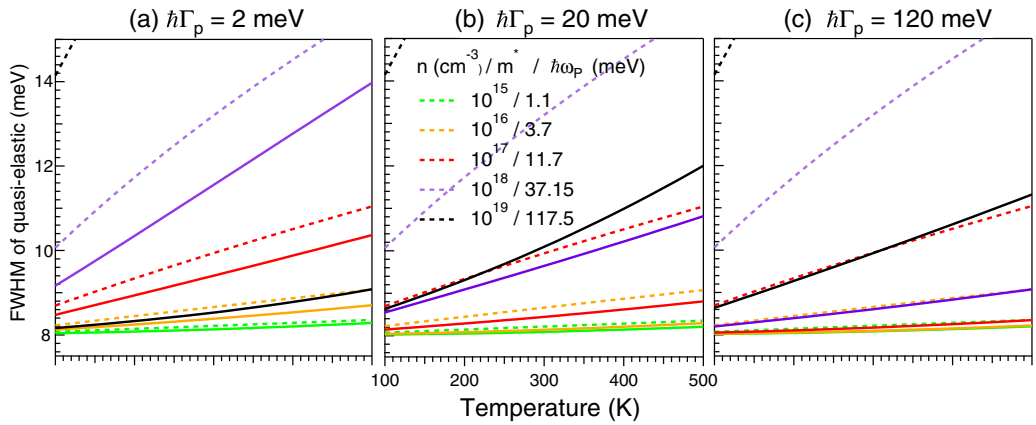

FIG. 5. Same as Fig. 4 (full lines) but as a function of temperature for various carrier densities n/m^* (or plasmon frequencies ω_P) and three different dampings: (a) $\hbar\Gamma_P = 2$ meV, (b) $\hbar\Gamma_P = 20$ meV, (c) $\hbar\Gamma_P = 120$ meV. Data are compared to the analytic results of Eq. (S3) in Supplemental Material [71] (dotted lines).

variable reduction states. As shown in Figs. 6–8, free carriers have a triple effect on phonon losses: (i) a broadening, (ii) a variation of relative intensities, and (iii) a shift toward higher frequency.

The broadening and change in intensity result from the existence of complex multiple and combination modes between surface phonon and plasmon excitations as demonstrated by the comparison of line profiles with [Fig. 6(b), Eq. (3)] and without [Fig. 6(c), Eq. (3); $n = 1$] multiple excitations. As seen in simulations at increased resolution ($\Delta_a \to 0$) and reduced dampings of both phonons and plasmon [108] ($\Gamma_{\rm LO}, \Gamma_{\rm TO}, \Gamma_P \to 0$), the single-loss spectrum [Fig. 6(c)] involves only the three main surface phonons $\omega_{\rm sph,1}$, $\omega_{\rm sph,2}$, $\omega_{\rm sph,3}$ (plus minor modes, Table S1 in Supplemental Material [71]) and a surface plasmon ω_{sp}. Upon including multiple excitations, the surface phonon $\omega_{\rm sph,3}$ around 100 meV is accompanied by side shoulders at $\omega_{\rm sph,3} \pm \omega_{sp}$. The resulting complex overall broadening follows roughly the trend of the quasielastic peak [Fig. 3(a)]. Indeed, if $\mathcal{P}(t) = \mathcal{P}_{Pl}(t) + \mathcal{P}_{Ph}(t)$ can be decomposed as the sum of isolated plasmon and phonon contributions [Eqs. (4) and (5)], then the full spectrum

$$P(\omega) = e^{-\mathcal{P}(0)} R(\omega) \otimes \left\{ \delta(\omega) + \sum_{n=1}^{\infty} \frac{1}{n!} [\mathcal{P}_{Pl}(\omega)]^{n\otimes} \right\} \otimes \left\{ \delta(\omega) + \sum_{n=1}^{\infty} \frac{1}{n!} [\mathcal{P}_{Ph}(\omega)]^{n\otimes} \right\} \quad (14)$$

appears as the convolution of the phonon multiple excitations by the plasmonic ones and vice versa. However, depending on the overlap in $\mathcal{P}(t)$, both excitations can even mix to generate the so-called "plasmaron" [39,40,109].

Regarding shifts, low-energy phonons at $\hbar\omega_{\rm sph,1} \simeq 45.2$ meV and $\hbar\omega_{\rm sph,2} \simeq 54.4$ meV are much less affected than the peak $\hbar\omega_{\rm sph,3} \simeq 92.9$ meV which is the focus of Fig. 7. This is particularly clear in Fig. 8 where fictitious spectra are plotted in the single-loss approximation at reduced damping; the shift, which directly stems from the screening of phonon excitation by carriers, correlates with the appearance of the surface plasmon feature close to the elastic peak. Up to a carrier density of $n/m^* \simeq 5 \times 10^{17}$ cm^{-3} ($\hbar\omega_P \simeq 20$ meV) (Figs. 7 and 8), $\hbar\omega_{\rm sph,3}$ keeps its unscreened value of 95.4 meV with a slight decrease in intensity due to broadening. Phonon intensity and Γ_P-induced broadening are strongly correlated [Fig. 7(b)]; the higher the plasmon damping Γ_P, the lower the intensity

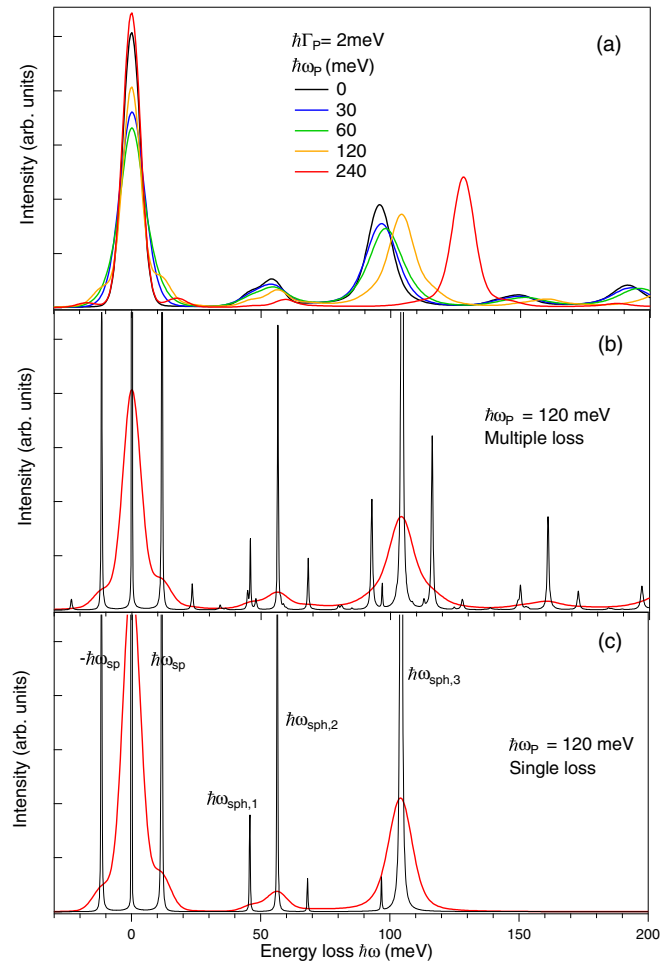

FIG. 6. (a) Evolution of the phonon energy-loss region with the plasmon frequency ω_P at fixed damping $\hbar\Gamma_P = 2$ meV. (b) Multiple and (c) single losses (red line) for the $\hbar\omega_P = 120$ meV case are compared to simulations at reduced phonon $\hbar\Gamma_{\rm TO} = \hbar\Gamma_{\rm LO} = 0.25$ meV and plasmon $\hbar\Gamma_P = 0.25$ meV dampings and increased resolution $\Delta_a = 0.25$ meV (black lines).

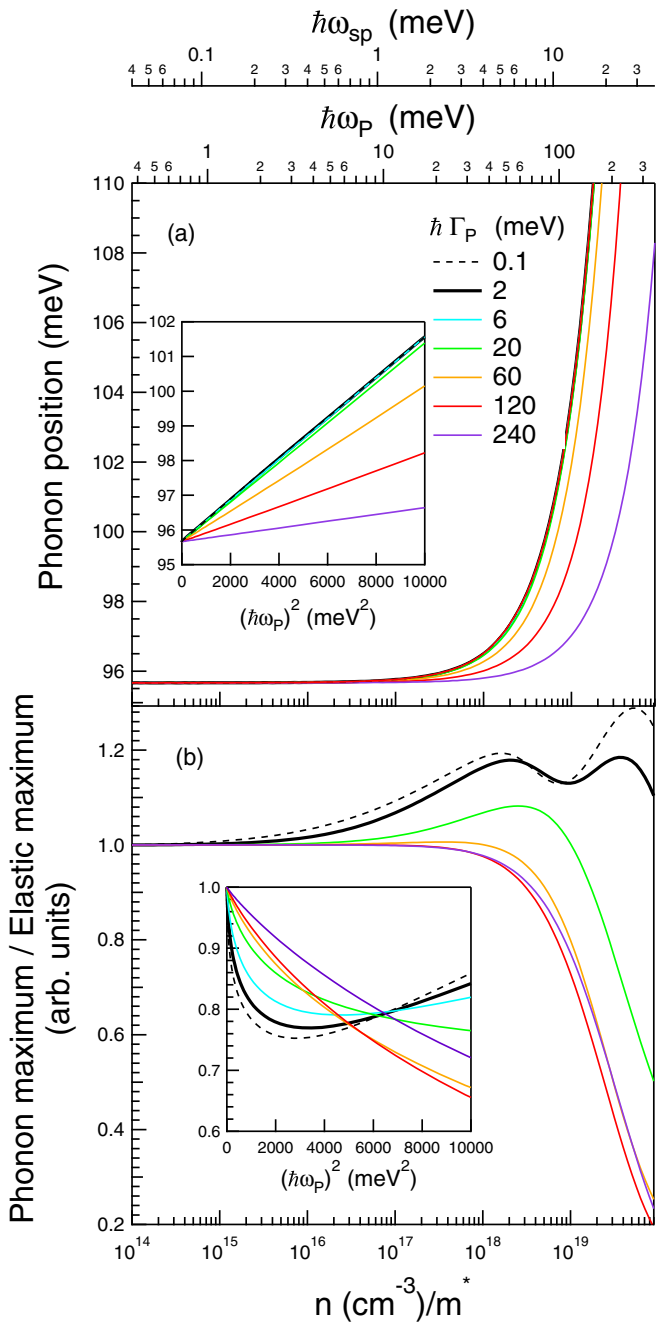

FIG. 7. Dependence on carrier density n/m^* (bottom scale) or plasmon frequencies ω_P, ω_{sp} (top scales) for various dampings Γ_P of the $\omega_{\mathrm{sph},3}$ phonon: (a) peak position and (b) peak intensity normalized to elastic intensity. Simulations include multiple excitations. The insets show the phonon position and its intensity as a function of $\omega_P^2 = ne^2/m_e m^* \epsilon_0$ once normalized to elastic.

as expected from the presence of $\omega_{\mathrm{sph},3} \pm \omega_{sp}$ peaks. Above $n/m^* \simeq 5 \times 10^{17}$ cm^{-3}, a noticeable shift is observed.

To first order, these findings can be rationalized in the single excitation regime by accounting for the high-energy phonon with a model of isolated oscillator of strength Ω, frequency ω_0, and damping Γ screened by a constant background ϵ_c:

$$\epsilon_{\mathrm{osc}}(\omega) = \epsilon_c + \frac{\Omega^2}{\omega_0^2 - \omega^2 - i\Gamma\omega}. \tag{15}$$

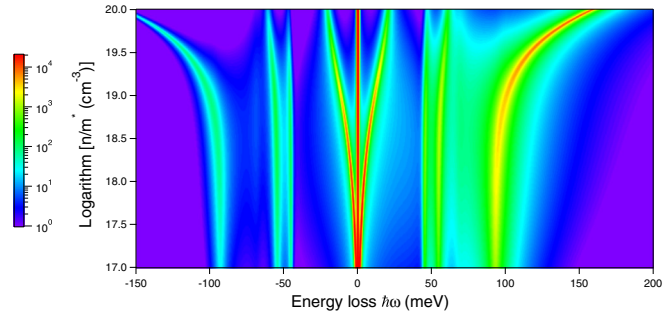

FIG. 8. Map of HREELS spectra in the single-loss approximation at enhanced resolution $\Delta_a = 1$ meV and poor phonon/plasmon damping $\hbar\Gamma = 1$ meV as a function of carrier density n/m^*. Notice the correlation between the appearance of the plasmon feature and the strong shift of the high-energy surface phonon $\omega_{\mathrm{sph},3}$.

Close to ω_0, the corresponding loss function

$$\mathrm{Im}\left[-\frac{1}{1+\xi_{\mathrm{osc}}(\omega)}\right] = \frac{\Gamma\omega\Omega^2}{\left[(1+\epsilon_c)\left(\omega_0^2-\omega^2\right)+\Omega^2\right]^2+\Gamma^2\omega^2(1+\epsilon_c)^2} \tag{16}$$

displays a quasi-Lorentzian shape [35] centered on ω_{osc}, of intensity I_{osc}, and of FWHM W_{osc} given by

$$\omega_{\mathrm{osc}} = \omega_0 + \frac{\Omega^2}{2\omega_0(1+\epsilon_c)}, \tag{17}$$

$$I_{\mathrm{osc}} = \frac{\Omega^2}{\Gamma\omega_0(1+\epsilon_c)^2}, \tag{18}$$

$$W_{\mathrm{osc}} = \frac{\Omega^2}{\omega_0(1+\epsilon_c)} - \Gamma. \tag{19}$$

In the case of plasmon (see Sec. III D), the screening constant at the oscillator frequency $\epsilon_c \simeq \epsilon_{c,0} - \omega_P^2/\omega_0^2$ decreases with the plasmon frequency below the value given by the remaining excitations $\epsilon_{c,0}$. For plasmon frequencies smaller than the oscillator eigenfrequency ω_0 or more precisely when $\omega_P \ll \omega_P^m = \omega_0\sqrt{1+\epsilon_{c,0}}$, a first-order expansion of Eqs. (17)–(19) shows that the frequency shift, the variation of intensity, and the width vary linearly with the carrier density $n \sim \omega_P^2$ with slopes α_P and β_P given by

$$\Delta\omega_{\mathrm{osc}} = \alpha_P\omega_P^2 = \frac{\Omega^2\omega_P^2}{2\omega_0^3(1+\epsilon_{c,0})^2}, \tag{20}$$

$$\Delta I_{\mathrm{osc}}/I_{\mathrm{osc}} = \beta_P\omega_P^2 = \frac{2\omega_P^2}{\omega_0^2(1+\epsilon_{c,0})^2}, \tag{21}$$

$$\Delta W_{\mathrm{osc}} = 2\alpha_P\omega_P^2 = \frac{\Omega^2\omega_P^2}{\omega_0^3(1+\epsilon_{c,0})^2}. \tag{22}$$

The estimated values of the corresponding parameters are given in Table S2 of Supplemental Material [71]. The linearity of the phonon shift with ω_P^2 is correctly verified below $(\omega_P^m)^2$ on full simulations (see insets of Fig. 7 for $\omega_{\mathrm{sph},3}$). However, the model remains qualitative. By using the oscillator strengths of Ref. [78] and $\epsilon_{c,0}$ obtained from the parametrization of Ref. [10], the values α_P (Table S2 in Supplemental Material [71]) of the slopes including all multiple excitations are systematically larger than those obtained through the screened

single isolated phonon. The discrepancy comes from the simplifying assumption of independent oscillators for phonons since a shift of a given peak significantly changes the screening of its neighbors; due to a larger oscillator strength, $\omega_{\mathrm{sph},3}$ is expected to shift faster than $\omega_{\mathrm{sph},2}$ which decreases its screening $\epsilon_{c,0}$ and therefore increases its α_P. The same reasoning applies to $\omega_{\mathrm{sph},1}$ and its neighbors at high energy $\omega_{\mathrm{sph},2}$. Anyway, according to Fig. 7(a), if all multiple excitations are taken into account, $\omega_{\mathrm{sph},3}$ is expected to shift by several meV, while increasing ω_P up to 100 meV and therefore the carrier concentration up to $n/m^* = 7.0 \times 10^{18}$ cm^{-3}.

C. Screening of phonons by band-gap states

The impact of BGS on polar phonons of TiO_2 was stressed in the earlier HREELS approaches [19,20,59] and in an indirect way in infrared study [66,67], as modification of the dielectric function at infinity ϵ_∞ for phonons [see Eq. (8), Sec. III A].

EELS spectra with a beam energy $E_I = 38$ eV and a resolution $\Delta_a = 50$ meV similar to experiments [22,69] have been calculated. As a first step, the BGS is represented by an oscillator [Eq. (11), Sec. III C] of strength Ω_{gs} spread homogeneously in a semi-infinite substrate [Fig. 9(a) inset]. It appears as a low-intensity feature between the phonon clump and the band-to-band transitions located above the 3.2-eV band gap of rutile. Aside from an obvious increase of its intensity with Ω_{gs}, the BGS shifts to higher energy [Figs. 9 and 11(a)] and gets asymmetric because of multiple excitations; in particular, a second-order excitation appears in the inset of Fig. 9(a) at around 2500 meV for $\hbar\Omega_{gs} = 2000$ meV. As shown by Eq. (17) for the simple oscillator used here to describe BGS, this shift roots into the EELS cross section which is proportional to $\mathrm{Im}[1/1+\epsilon(\omega)]$ and is linear in Ω_{gs}^2 modulo the sensitivity function as shown in Fig. 11(a).

In contrast to interband transitions which seem insensitive to BGS because of their much smaller oscillator strengths, the phonon region is strongly screened by BGS. The effect is fairly well illustrated in high-resolution spectrum including [Fig. 9(a)] or not (Fig. 10) multiple losses, but it is less obvious at moderate resolution as usually used in EELS [Fig. 9(a), inset]. Phonons evolve in the opposite direction with respect to the screening induced by carrier excitations; they all redshift and the $\omega_{\mathrm{sph},3}$ intensity decreases [Fig. 11(b)]. Phonon screening by the tail of BGS excitation is again the main driving force. But, since the frequency of BGS is larger than those of phonons, the real part of the BGS dielectric component $\epsilon_{gs}(\omega)$ is negative at phonon frequencies (Fig. 1) at the opposite to the plasmon contribution $\epsilon_{pl}(\omega)$. The effect can also be accounted by describing phonons through isolated oscillators to determine variations in position and intensity. To first order, i.e., $\Omega_{gs} \ll \omega_{gs}^m = \omega_{gs}\sqrt{1+\epsilon_{c,0}}$, they are linear in Ω_{gs}^2 with negative slopes that amount to

$$\Delta\omega_{\mathrm{osc}} = -\alpha_{gs}\Omega_{gs}^2 = -\frac{\Omega^2\Omega_{gs}^2}{2\omega_0\omega_{gs}(1+\epsilon_{c,gs})^2}, \quad (23)$$

$$\Delta I_{\mathrm{osc}}/I_{\mathrm{osc}} = -\beta_{gs}\Omega_{gs}^2 = -\frac{2\Omega_{gs}^2}{\omega_{gs}^2(1+\epsilon_{c,gs})^2}, \quad (24)$$

$$\Delta W_{\mathrm{osc}} = -2\alpha_{gs}\Omega_{gs}^2 = -\frac{\Omega^2\Omega_{gs}^2}{\omega_0\omega_{gs}(1+\epsilon_{c,gs})^2}. \quad (25)$$

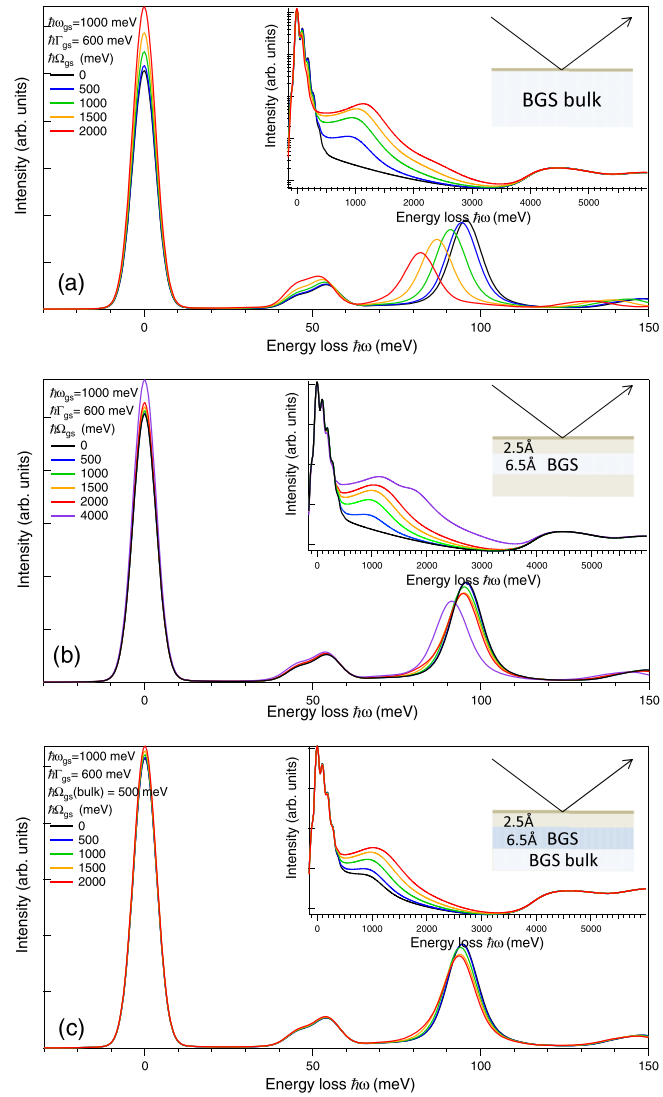

FIG. 9. Evolution of the phonon (main graphs, linear scale) and band-gap (insets, logarithmic scale) electron energy-loss spectra as a function of the band-gap state strength Ω_{gs} (at constant frequency $\hbar\omega_{gs} = 1000$ meV and damping $\hbar\Gamma_{gs} = 600$ meV): (a) semi-infinite substrate, (b) BGS localized in a layer thickness 6.5 Å just below the surface, and (c) mixture of both configurations with $\hbar\omega_{gs}^{bulk} = 500$ meV. Dielectric profile is chosen accordingly to the experimental findings [22,69].

Downward shifts and decrease in phonon intensities obtained in the case of multiple excitations [Fig. 11(b)] are well accounted for. The limits of the modeling by isolated oscillators and single loss explain the quantitative discrepancy between calculated slopes α_{gs}, β_{gs} and actual values (Table S2 in Supplemental Material [71] for numerical values).

Surprisingly, the BGS also impacts the quasielastic peak intensity which increases at constant FWHM [Fig. 11(a)] with Ω_{gs}. This phenomenon finds its origin in the transfer of intensity from phonons and their multiple excitations to the elastic contribution of the quasielastic peak. Therefore, once normalized to the elastic peak, phonons decrease in intensity upon increasing the BGS strength [Fig. 11(b), inset]. This relative variation of phonon/elastic appears in an obvious way

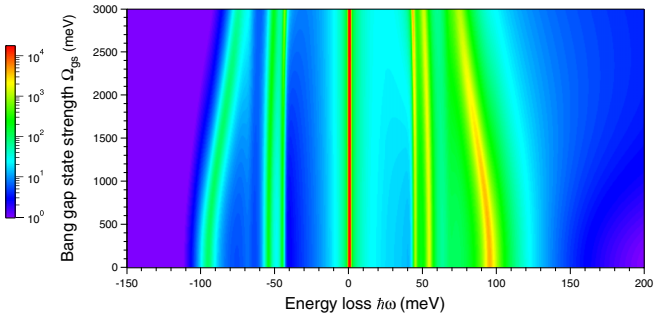

FIG. 10. Map of HREELS spectra of phonons in the single-loss approximation at enhanced resolution $\Delta_a = 1$ meV and poor phonon/plasmon damping $\hbar\Gamma = 1$ meV as a function of band-gap state strength Ω_{gs}. A clear downward shift of the surface phonons, in particular $\omega_{\mathrm{sphn},3}$, is observed.

on experimental spectra during healing of defects by oxygen exposure [69].

V. EELS DEPTH SENSITIVITY AND THE PROFILE OF DIELECTRIC FUNCTION

Up to now, the discussion was restricted to a semi-infinite substrate. The profile of dielectric function related to defects was not accounted for. However, while both surface oxygen vacancies and titanium interstitials contribute to BGS in TiO_2 [22], excess electrons were shown to be localized on subsurface titanium by resonant photoemission [16] and further confirmed by out-of-specular EELS [22]. In this context, the variable depth sensitivity of EELS in dipolar regime as a function of impact and loss energies is of interest. A fair estimate of probing depth [35,50] is the evanescent decay length d_p of the electric field due to the incoming electron which is given by the inverse of the electron wave-vector transfer $d_p \simeq 1/k_\parallel = 1/(k_S - k_I)\sin\Theta_I \simeq 1/(k_I\theta_E \sin\Theta_I)$. d_p has been plotted in Fig. 12 for two beam energies $E_I = 8$ and 38 eV, typical for loss regimes of phonons and BGS and compared to values averaged over the detector aperture [22]. The higher the beam energy and the lower the energy loss, the deeper the probing depth. Measurements are bulk sensitive

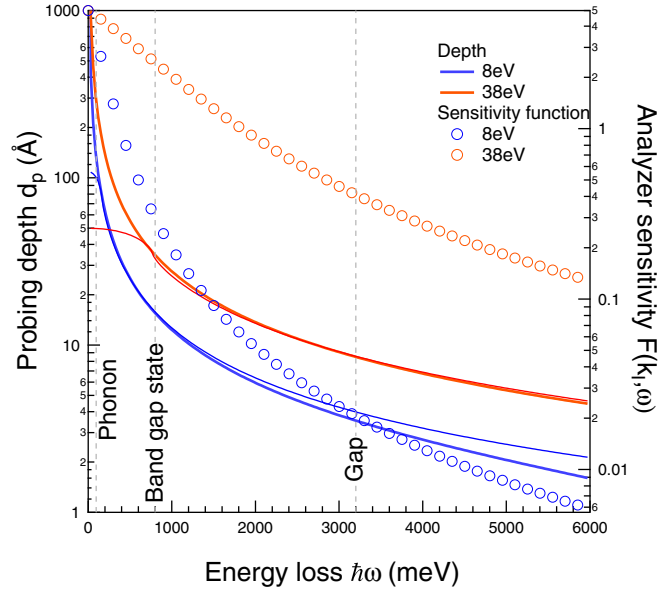

FIG. 12. Probing depths (left scale) and analyzer sensitivity function (right scale) for two beam energies $E_I = 8$ eV and 38 eV. The basic estimate d_p (thick lines) is compared to the average $\langle d_p \rangle$ over a circular slit of aperture $\theta_c = 1^\circ$ (thin lines). The main effect of slit integration is to smoothen the divergence at $\hbar\omega = 0$ [22]. Phonon, band-gap state, and band gap of TiO_2 are shown by dotted lines. Notice that d_p was also calculated well outside the regime of negligible loss at $E_I = 8$ eV.

for phonons ($d_p \simeq 200$ Å), not speaking about quasielastic excitations. Conversely, EELS at $E_I = 38$ eV that probes the subsurface at the BGS energy ($d_p \simeq 30$ Å) becomes very surface sensitive for interband transition ($d_p < 10$ Å).

But, caution is required for detailed analysis since the depth dependence of EELS cross section is quite complex. For instance, while it corresponds to a constant dielectric function, the sensitivity function $F(E_I, \cos\Theta_I, \omega)$ that takes into account the scattering geometry [35] [Eq. (1)] does not follow the $d_p(\omega)$ trend (Fig. 12; symbols vs lines). A better definition of d_p must account for the weight given for each $k_\parallel$ by the sensitivity function [50] and for the $k_\parallel$ dependence

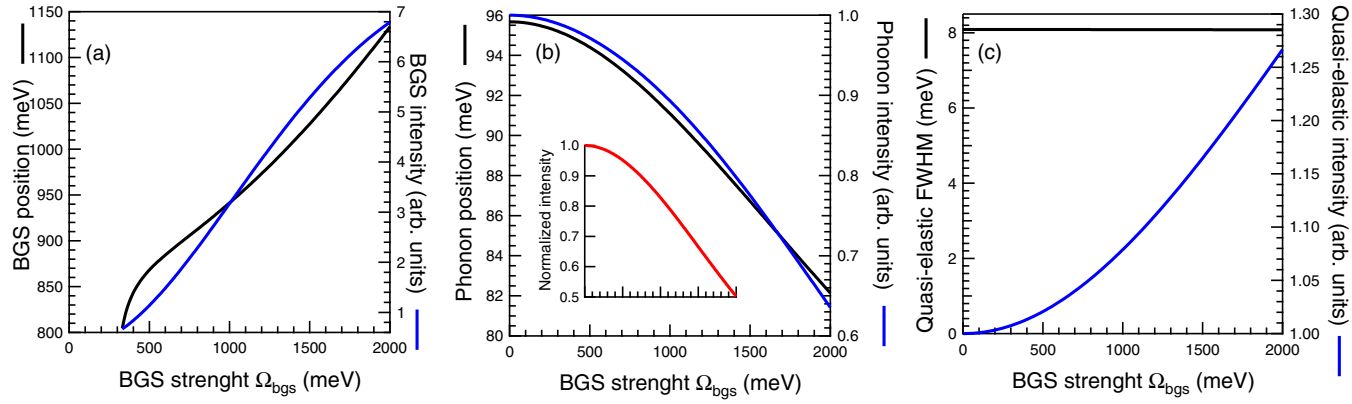

FIG. 11. Variation with the band-gap state strength Ω_{gs} of the peak intensities, positions or FWHMs of the (a) BGS, (b) phonon, and (c) elastic peak. Notice that BGS is a maximum-less shoulder below a critical Ω_{gs} value. The phonon intensity normalized to the elastic intensity is shown in inset of (b). All multiple losses have been accounted for.

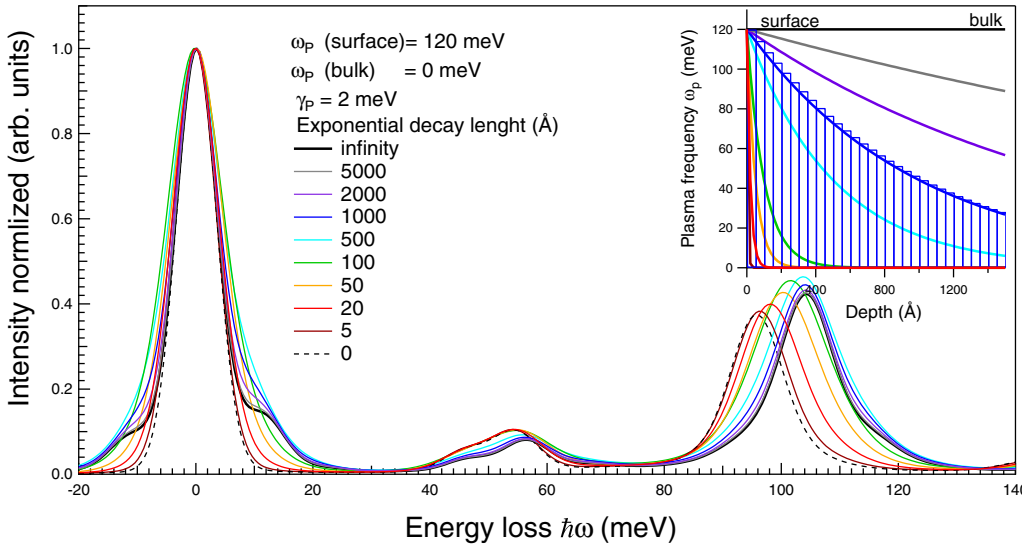

FIG. 13. Effect of an exponential gradient of carrier density (shown in inset) on the HREELS phonon spectrum in the absence of BGS contribution. The plasma frequency goes from $\hbar\omega_P = 120$ meV at the surface to $\hbar\omega_P = 0$ meV in the bulk while the damping is taken constant equal to $\hbar\Gamma_P = 2$ meV. The exponential decay length goes from 0 Å to infinity, i.e., from an undoped substrate to flat profile. The profile is sampled over 60 slices in-between 0 and 3Λ as illustrated by the blue staircase curve for $\Lambda = 1000$ Å. Spectra are normalized to the elastic peak maximum.

of the loss function $G(k_\parallel, \omega)$ [Eq. (1)] which expression is already complex for a stratified medium [58] [Eq. (S2) in Supplemental Material [71]]. Therefore, it is mandatory to resort to full numerical simulations to accurately discuss depth sensitivity effects and profile of dielectric function, as shown in the following three examples.

In Fig. 9, several models of distribution of BGS [bulk: Fig. 9(a), subsurface: Fig. 9(b), and mixture of both: Fig. 9(c)] have been compared at increasing BGS oscillator strength. As shown in the schematic profiles in insets, subsurface BGS are put in a 6.5-Å-thick layer below a 2.5-Å dead layer to mimic the localization of charge on subsurface Ti atoms at rutile TiO_2(110) [16,22]. The sizable impact of bulk BGS on phonon position and on relative intensity to elastic peak [Fig. 9(a)] is considerably damped for a subsurface excitation despite a similar intensity as a band-gap feature in EELS [Fig. 9(b)]. This effect finds its origin in the difference of probing depth between excitations at phonon and band-gap state energies (Fig. 12). In a similar way, the barely visible bulk BGS excitation buried at a depth below $6.5 + 2.5 = 9$ Å [Fig. 9(c); black line in inset] strongly shifts the main phonon peak [Figs. 9(b) and 9(c); black lines].

Figure 13 illustrates the more complex dielectric function profile of an exponential decaying gradient of carriers from a surface value $\hbar\omega_P = 120$ meV to a bulk value $\hbar\omega_P = 0$ meV, which could mimic an accumulation layer due to band bending and charge transfer with surface defects. The profile was sampled in a staircase way (inset of Fig. 13) over three times the decay length Λ and the loss function computed recursively [Eq. (S2) in Supplemental Material [71]]. The effects on the quasielastic peak, the phonon position, and their relative ratio parallels the trends described in Secs. IV B and IV C for a semi-infinite sample. Interestingly, the spectrum poorly evolves between $\Lambda = 2000$ Å (violet curve) and a bulk substrate (bold black line) in the phonon range, while sizable differences are still visible for the quasielastic peak. The explanation lies in the difference of probing depth (see Fig. 12) at the two energies. The sensitivity to such high Λ values for phonons compared to the expected probing depth $d_p \simeq 200$ Å comes from the initial difference of slopes of $\omega_P(z)$; this means that a linear profile would give a quite similar spectrum.

The last example (Fig. 14) deals with a fictitious highly conductive layer ($\hbar\Gamma_p = 2$ meV) of thickness ($t = 6.5$ Å) equivalent to the distance between Ti planes in TiO_2(110) buried at increasing depth below the surface. Its plasma frequency $\hbar\omega_P = 500$ meV corresponds to a surface carrier density of $n_S/m^* = 1.2 \times 10^{13}$ cm^2 typical for a doping by a fraction of monolayer of defects. This layer impacts the phonon position $\omega_{\mathrm{sph},3}$ down to around the expected probing depth of $1/k_\parallel = d_p \simeq 200$ Å, but the peak intensity is not yet converged. The surface plasmon excitation confined in this

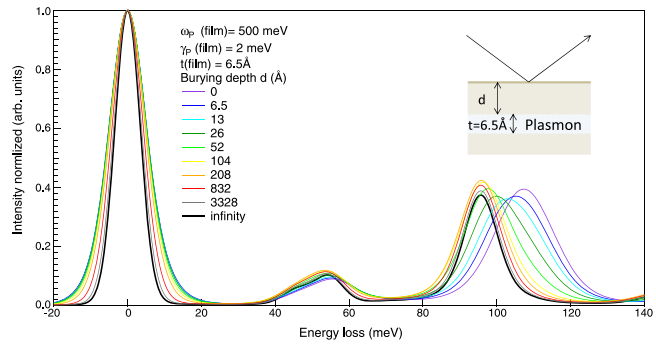

FIG. 14. Effect of a conductive layer ($\hbar\omega_P = 500$ meV, $\hbar\Gamma_p = 2$ meV, $t = 6.5$ Å) buried at different depth d on the HREELS phonon spectrum (see inset). Spectra are normalized to the elastic peak maximum.

layer is still able to broaden the quasielastic peak up to a rather large burying depth.

These few theoretical examples highlight the sensitivity of EELS to profiles of dielectric function and the complexity of interplay between excitations.

VI. CONCLUSION

Based on an accurate buildup of the dielectric function from far infrared to ultraviolet, the interplay between the solid-state excitations of reduced TiO_2 rutile was explored in the frame of the EELS dipole scattering theory. While the contributions from optical phonons and interband transitions were extracted from literature, the transport of excess electrons was described through a Drude model and the associated band-gap states through an oscillator. The analysis showed that the dielectric anisotropy has a minor impact due to a fortuitous degeneracy of phonon modes. Upon increasing the carrier concentration or the plasma frequency and contrary to most semiconductors, only a modest broadening of the quasielastic peak is expected because of the large static dielectric function and effective mass in TiO_2. Only in the most extreme case, a surface plasmon shoulder on the side of the quasielastic peak is to be detected. Nevertheless, carriers should induce a measurable temperature dependence of this latter.

Conversely, band-gap states appear clearly as isolated features. Due to its large oscillator strength, the surface phonon around 95 meV can be used as a reliable reporter of the excess electron excitations through the screenings they induce. Above a carrier concentration of 10^{17}–10^{18} cm^{-3}, an upward shift is predicted. However, it should be counterbalanced by a downward shift due to band-gap states oscillator strength. Both plasmon and BGS impact the ratio of phonon to elastic peak by pumping out intensity. If the screening effect can be rationalized through an isolated oscillator model of phonons, the accurate description of shifts, variations of intensity, or broadenings of phonons and elastic peak requires a full account of all excitations. At last, while probing depth is much larger for the quasielastic peak and phonons than for band-gap states, the previous trends obtained for semi-infinite substrate hold true for various dielectric profiles. But, their account turns out to be mandatory for quantitative analysis.

The present conclusions on phonon screening in EELS can be generalized to any reducible oxide showing polaronic defect states since a high static dielectric constant is often related to longitudinal phonon modes of high oscillator strengths.

[1] J. Jupille and G. Thornton, *Defects at Oxide Surfaces* (Springer, Berlin, 2015).
[2] U. Diebold, Surf. Sci. Rep. **48**, 53 (2003).
[3] C. Lun Pang, R. Lindsay, and G. Thornton, Chem. Soc. Rev. **37**, 2328 (2008).
[4] L.-M. Liu, P. Crawford, and P. Hu, Prog. Surf. Sci. **84**, 155 (2009).
[5] Z. Dohnálek, I. Lyubinetsky, and R. Rousseau, Prog. Surf. Sci. **85**, 161 (2010).
[6] M. A. Henderson, Surf. Sci. Rep. **66**, 185 (2011).
[7] C. L. Pang, R. Lindsay, and G. Thornton, Chem. Rev. **113**, 3887 (2013).
[8] M. A. Henderson and I. Lyubinetsky, Chem. Rev. **113**, 4428 (2013).
[9] W.-J. Yin, B. Wen, C. Zhou, A. Selloni, and L. M. Liu, Surf. Sci. Rep. **73**, 58 (2018).
[10] D. Schöche, T. Hofmann, R. Korlacki, T. Tiwald, and M. Schubert, J. Appl. Phys. **113**, 164102 (2013).
[11] D. Emin, Phys. Rev. B **48**, 13691 (1993).
[12] A. Fujimori, A. E. Bocquet, K. Morikawa, K. Kobayashi, I. T. Saithoh, Y. Tokura, I. Hasex, and M. Onoda, J. Phys. Chem. Solids **57**, 1379 (1996).
[13] G. Mattioli, P. Alippi, F. Filippone, R. Caminiti, and A. A. Bonapasta, J. Phys. Chem. C **114**, 21694 (2010).
[14] V. E. Henrich, G. Dresselhaus, and H. J. Zeiger, Phys. Rev. Lett. **36**, 1335 (1976).
[15] R. Kurtz, R. Stockbauer, T. Madey, E. Román, and J. de Segovia, Surf. Sci. **218**, 178 (1989).
[16] P. Krüger, S. Bourgeois, B. Domenichini, H. Magnan, D. Chandesris, P. Le Fèvre, A. M. Flank, J. Jupille, L. Floreano, A. Cossaro, A. Verdini, and A. Morgante, Phys. Rev. Lett. **100**, 055501 (2008).
[17] C. M. Yim, C. L. Pang, and G. Thornton, Phys. Rev. Lett. **104**, 036806 (2010).
[18] P. Borghetti, E. Meriggio, G. Rousse, G. Cabailh, R. Lazzari, and J. Jupille, J. Phys. Chem. Lett. **7**, 3223 (2016).
[19] G. Rocker, J. A. Schaefer, and W. Göpel, Phys. Rev. B **30**, 3704 (1984).
[20] S. Eriksen and R. G. Egdell, Surf. Sci. **180**, 263 (1987).
[21] W. S. Epling, C. H. F. Peden, M. A. Henderson, and U. Diebold, Surf. Sci. **412-413**, 333 (1998).
[22] J. Li, R. Lazzari, S. Chenot, and J. Jupille, Phys. Rev. B **97**, 041403(R) (2018).
[23] A. C. Papageorgiou, N. S. Beglitis, C. L. Pang, G. Teobaldi, G. Cabailh, Q. Chen, A. J. Fisher, W. A. Hofer, and G. Thornton, Proc. Natl. Acad. Sci. USA **107**, 2391 (2010).
[24] M. Setvin, C. Franchini, X. Hao, M. Schmid, A. Janotti, M. Kaltak, C. G. Van de Walle, G. Kresse, and U. Diebold, Phys. Rev. Lett. **113**, 086402 (2014).
[25] V. Bogomolov and D. Mirlin, Phys. Status Solidi **27**, 443 (1968).
[26] V. M. Khomenko, K. Langer, H. Rager, and A. Fett, Phys. Chem. Miner. **25**, 338 (1998).
[27] M. Chiesa, M. Paganini, S. Livraghi, and E. Giamello, Phys. Chem. Chem. Phys. **15**, 9435 (2013).
[28] L. Hollander and P. L. Castro, Phys. Rev. **119**, 1882 (1960).
[29] J. H. Becker and W. R. Hosler, Phys. Rev. **137**, A1872 (1965).
[30] E. Iguchi, K. Yajima, T. Asahina, and Y. Kanamori, J. Phys. Chem. Solids **35**, 597 (1974).
[31] E. Yagi, R. R. Hasiguti, and M. Aono, Phys. Rev. B **54**, 7945 (1996).
[32] E. Hendry, F. Wang, J. Shan, T. F. Heinz, and M. Bonn, Phys. Rev. B **69**, 081101(R) (2004).
[33] P. M. Kowalski, M. F. Camellone, N. N. Nair, B. Meyer, and D. Marx, Phys. Rev. Lett. **105**, 146405 (2010).

[34] A. Janotti, C. Franchini, J. B. Varley, G. Kresse, and C. G. Van de Walle, *Dual Behavior of Excess Electrons in Rutile* TiO_2, Vol. 7 (Wiley, Hoboken, NJ, 2013), pp. 199–203.

[35] H. Ibach and D. L. Mills, *Electron Energy Loss Spectroscopy and Surface Vibrations* (Academic, New York, 1982).

[36] L. Vattuone, L. Savio, and M. Rocca, *Surface Science Techniques* (Springer, Berlin, 2013), pp. 499–529.

[37] H. Ibach, Phys. Rev. Lett. **24**, 1416 (1970).

[38] P. Lambin, L. Henrard, P. Thiry, C. Silien, and J. P. Vigneron, J. Electron Spectrosc. Relat. Phenom. **129**, 281 (2003).

[39] Y. Goldstein, A. Many, and I. Wagner, Surf. Sci. **98**, 599 (1980).

[40] A. Many, I. Wagner, A. Rosenthal, J. I. Gersten, and Y. Goldstein, Phys. Rev. Lett. **46**, 1648 (1981).

[41] Y. Wang, B. Meyer, X. Yin, M. Kunat, D. Langenberg, F. Traeger, A. Birkner, and C. Wöll, Phys. Rev. Lett. **95**, 266104 (2005).

[42] H. Qiu, B. Meyer, Y. Wang, and C. Wöll, Phys. Rev. Lett. **101**, 236401 (2008).

[43] B. N. J. Persson and J. E. Demuth, Phys. Rev. B **30**, 5968 (1984).

[44] J. A. Stroscio and W. Ho, Phys. Rev. Lett. **54**, 1573 (1985).

[45] J. A. Stroscio and W. Ho, Phys. Rev. B **36**, 9736 (1987).

[46] A. Ritz and H. Lüth, Phys. Rev. Lett. **52**, 1242 (1984).

[47] T. Inaoka and D. M. Newns, Surf. Sci. **186**, 290 (1987).

[48] Y. Chen, J. C. Hermanson, and G. J. Lapeyre, Phys. Rev. B **39**, 12682 (1989).

[49] R. Matz and H. Lüth, Phys. Rev. Lett. **46**, 500 (1981).

[50] M. Noguchi, K. Hirakawa, and T. Ikoma, Surf. Sci. **271**, 260 (1992).

[51] V. M. Polyakov, A. Elbe, J. Wu, G. J. Lapeyre, and J. A. Schaefer, Phys. Rev. B **54**, 2010 (1996).

[52] A. A. Lucas and M. Sunjić, Phys. Rev. Lett. **26**, 229 (1971).

[53] A. A. Lucas and M. Sunjić, Prog. Surf. Sci. **2**, 75 (1972).

[54] E. Evans and D. L. Mills, Phys. Rev. B **5**, 4126 (1972).

[55] E. Evans and D. L. Mills, Phys. Rev. B **7**, 853 (1973).

[56] D. L. Mills, Surf. Sci. **48**, 59 (1975).

[57] A. A. Lucas and J. P. Vigneron, Solid State Commun. **49**, 327 (1984).

[58] P. Lambin, J. P. Vigneron, and A. A. Lucas, Phys. Rev. B **32**, 8203 (1985).

[59] P. A. Cox, R. G. Edgell, S. Eriksen, and W. R. Flavell, J. Electron Spectrosc. Relat. Phenom. **39**, 117 (1986).

[60] L. L. Kesmodel, J. A. Gates, and Y. W. Chung, Phys. Rev. B **23**, 489 (1981).

[61] M. A. Henderson, Surf. Sci. **355**, 151 (1996).

[62] M. A. Henderson, W. S. Epling, C. L. Perkins, C. H. F. Peden, and U. Diebold, J. Phys. Chem. B **103**, 5328 (1999).

[63] M. A. Henderson, W. S. Epling, C. H. F. Peden, and C. L. Perkins, J. Phys. Chem. B **107**, 534 (2003).

[64] M. A. Henderson, M. Shen, Z.-T. Wang, and I. Lyubinetsky, J. Phys. Chem. C **117**, 5774 (2013).

[65] H. Noei, L. Jin, H. Qiu, M. Xu, Y. Gao, J. Zhao, M. Kauer, C. Wöll, M. Muhler, and Y. Wang, Phys. Status Solidi B **250**, 1204 (2013).

[66] F. Gervais and J. F. Baumard, Solid State Commun. **21**, 861 (1977).

[67] J. F. Baumard and F. Gervais, Phys. Rev. B **15**, 2316 (1977).

[68] P. A. Thiry, M. Liehr, J.-J. Pireaux, and R. Caudano, Phys. Scr. **35**, 368 (1987).

[69] J. Li, Origin, location and transport of excess charges in titanium dioxide, Ph.D. thesis, Pierre and Marie Curie University, France, 2016.

[70] W. Schaich, Surf. Sci. **122**, 175 (1982).

[71] See Supplemental Material at http://link.aps.org/supplemental/10.1103/PhysRevB.98.075432 for a description (i) of the dielectric theory of EELS of uniaxial material and graded interface (Sec. S1), (ii) of the effect of anisotropy (Sec. S2), (iii) of the analytic equation of plasmon-induced broadening of the quasielastic peak (Sec. S3), and (iv) for complementary figures and tables (Sec. S4).

[72] P. A. Cox, W. R. Flavell, A. A. Williams, and R. G. Egdell, Surf. Sci. **152-153**, 784 (1985).

[73] R. Piessens, E. deDoncker Kapenga, C. Uberhuber, and D. Kahaner, *Quadpack: a Subroutine Package for Automatic Integration*, Springer Series in Computational Mathematics Vol. 1 (Springer, Berlin, 1983).

[74] H. Ibach, *Electron Energy Loss Spectrometers: The Technology of High Performance* (Springer, Berlin, 1991).

[75] E. D. Palik, *Handbook of Optical Constants of Solids*, Vols. 1–3 (Academic, New York, 1985).

[76] F. Gervais and B. Piriou, Phys. Rev. B **10**, 1642 (1974).

[77] F. Gervais, Mater. Sci. Eng., R **39**, 29 (2002).

[78] D. M. Eagles, J. Phys. Chem. Solids **25**, 1243 (1964).

[79] J. G. Traylor, H. G. Smith, R. M. Nicklow, and M. K. Wilkinson, Phys. Rev. B **3**, 3457 (1971).

[80] C. Lee, P. Ghosez, and X. Gonze, Phys. Rev. B **50**, 13379 (1994).

[81] P. D. Mitev, K. Hermansson, B. Montanari, and K. Refson, Phys. Rev. B **81**, 134303 (2010).

[82] M. Dou and C. Persson, J. Appl. Phys. **113**, 083703 (2013).

[83] D. Schöche (private communication).

[84] R. Betsch, H. Park, and W. White, Mater. Res. Bull. **26**, 613 (1991).

[85] N. W. Aschcroft and N. D. Mermin, *Physique des Solides* (EDP Sciences, Les Ulis, France, 2002).

[86] G. Samara and P. Peercy, Phys. Rev. B **7**, 1131 (1973).

[87] J. Pascual, J. Camassel, and H. Mathieu, Phys. Rev. B **18**, 5606 (1978).

[88] L. Chiodo, J. M. García-Lastra, A. Iacomino, S. Ossicini, J. Zhao, H. Petek, and A. Rubio, Phys. Rev. B **82**, 045207 (2010).

[89] N. Vast, L. Reining, V. Olevano, P. Schattschneider, and B. Jouffrey, Phys. Rev. Lett. **88**, 037601 (2002).

[90] I. G. Gurtubay, W. Ku, J. M. Pitarke, A. G. Eguiluz, B. C. Larson, J. Tischler, and P. Zschack, Phys. Rev. B **70**, 201201 (2004).

[91] J. Leng, J. Opsala, H. Chua, M. Senkoa, and D. Aspnes, Thin Solid Films **313-314**, 132 (1998).

[92] A. Djurisic, Y. Chan, and E. Li, Mater. Sci. Eng., R **38**, 237 (2002).

[93] J. T. Devreese and A. S. Alexandrov, Rep. Prog. Phys. **72**, 066501 (2009).

[94] A. S. Alexandrox and J. Devreese, *Advances in Polaron Physics* (Springer, Heidelberg, 2010).

[95] K. Onda, B. Li, and H. Petek, Phys. Rev. B **70**, 045415 (2004).

[96] S. Wendt, P. T. Sprunger, E. Lira, G. K. H. Madsen, Z. Li, J. O. Hansen, J. Matthiesen, A. Blekinge-Rasmussen, E. Laegsgaard, B. Hammer, and F. Besenbacher, Science **320**, 1755 (2008).

[97] K. Mitsuhara, H. Okumura, A. Visikovskiy, M. Takizawa, and Y. Kido, J. Chem. Phys. **136**, 124707 (2012).
[98] X. Mao, X. Lang, Z. Wang, Q. Hao, B. Wen, Z. Ren, D. Dai, C. Zhou, L. M. Liu, and X. Yang, J. Phys. Chem. Lett. **4**, 3839 (2013).
[99] T. Minato, Y. Sainoo, Y. Kim, H. S. Kato, K. Aika, M. Kawai, J. Zhao, H. Petek, T. Huang, W. He, W. Bing, W. Zhuo, Y. Zhao, J. Yang, and J. G. Hou, J. Chem. Phys. **130**, 124502 (2009).
[100] S. Moser, L. Moreschini, J. Jaćimović, O. S. Barišić, H. Berger, A. Magrez, Y. J. Chang, K. S. Kim, A. Bostwick, E. Rotenberg, L. Forró, and M. Grioni, Phys. Rev. Lett. **110**, 196403 (2013).
[101] C. Verdi, F. Caruso, and F. Giustino, Nat. Commun. **8**, 15769 (2017).
[102] T. He, Phys. Rev. B **51**, 16689 (1995).
[103] P. G. Moses, A. Janotti, C. Franchini, G. Kresse, and C. G. Van de Walle, J. Appl. Phys. **119**, 181503 (2016).
[104] R. R. Hasiguti and E. Yagi, Phys. Rev. B **49**, 7251 (1994).
[105] E. Hendry, M. Koeberg, J. Pijpers, and M. Bonn, Phys. Rev. B **75**, 233202 (2007).
[106] F. Herklotz, E. V. Lavrov, and J. Weber, Phys. Rev. B **83**, 235202 (2011).
[107] J. D. Jackson, *Classical Electrodynamics* (Wiley, New York, 1975).
[108] R. Lazzari, J. Li, and J. Jupille, Rev. Sci. Instrum. **86**, 013906 (2015).
[109] J. I. Gersten, Surf. Sci. **92**, 579 (1980).